The Astrophysical Journal, 899:116 (10pp), 2020 August 20 https://doi.org/10.3847/1538-4357/aba748

The Contour Method: a New Approach to Finding Modes of Nonadiabatic Stellar Pulsations

J. Goldstein[1,2] and R. H. D. Townsend[1,2]
[1] Department of Astronomy, University of Wisconsin-Madison, 2535 Sterling Hall, 475 N. Charter Street, Madison, WI 53706, USA; jgoldstein@astro.wisc.edu
[2] Kavli Institute for Theoretical Physics, University of California, Santa Barbara, CA 93106, USA
Received 2020 June 30; revised 2020 July 17; accepted 2020 July 17; published 2020 August 19

Abstract

The contour method is a new approach to calculating the nonadiabatic pulsation frequencies of stars. These frequencies can be found by solving for the complex roots of a characteristic equation constructed from the linear nonadiabatic stellar pulsation equations. A complex-root solver requires an initial trial frequency for each nonadiabatic root. A standard method for obtaining initial trial frequencies is to use a star's adiabatic pulsation frequencies, but this method can fail to converge to nonadiabatic roots, especially as the growth and/or damping rate of the pulsations becomes large. The contour method provides an alternative way to obtain initial trial frequencies that robustly converges to nonadiabatic roots, even for stellar models with extremely nonadiabatic pulsations and thus high growth/damping rates. We describe the contour method implemented in the GYRE stellar pulsation code and use it to calculate the nonadiabatic pulsation frequencies of 10 $M_\odot$ and 20 $M_\odot$ β Cephei star models, and of a 0.9 $M_\odot$ extreme helium star model.

Unified Astronomy Thesaurus concepts: Asteroseismology (73); Stellar oscillations (1617); Computational methods (1965); Astronomy software (1855)

1. Introduction

Stars across the Hertzsprung–Russel diagram (HRD) exhibit pulsations that carry information about stellar structure and evolution. Modeling stellar pulsations requires solving the stellar pulsation equations (e.g., Unno et al. 1989; Aerts et al. 2010) as a boundary eigenvalue problem, to obtain eigenfrequencies and eigenfunctions. Many stellar pulsation codes solve for eigenfrequencies by finding the roots of a characteristic equation,

$$\mathcal{D}(\sigma) = 0, \tag{1}$$

where $\mathcal{D}(\sigma)$ is a discriminant function, and σ is the pulsation angular frequency. Pulsation codes approach constructing discriminant functions in different ways, and even the same code can implement a variety of approaches; but the roots should agree within and across codes because they represent the intrinsic eigenfrequencies of the star.

How pulsation codes construct and solve the characteristic equation depends on whether the pulsations being modeled are adiabatic or nonadiabatic. For adiabatic pulsations, the linear adiabatic (LA) stellar pulsation equations yield $\mathcal{D}(\sigma)$ and σ that are real-valued, and the roots are guaranteed to be found through standard bracketing approaches such as bisection (e.g., Press et al. 1992).

For nonadiabatic pulsations, the linear nonadiabatic (LNA) stellar pulsation equations yield $\mathcal{D}(\sigma)$ and σ that are complex-valued. The pulsation frequency can be written

$$\sigma = \sigma_R + i\sigma_I, \tag{2}$$

where "R" and "I" denote real and imaginary parts, respectively. When we assume that pulsations have a time dependence $\propto\exp(-i\sigma t)$, σ_R describes the oscillatory behavior of the pulsation, while σ_I describes overstable growth ($\sigma_I > 0$) or damped decay ($\sigma_I < 0$).

Complex roots cannot meaningfully be bracketed; therefore, solving the characteristic Equation (1) in the LNA case requires iterative improvement of an initial trial frequency, using, for instance, the Newton–Raphson or secant algorithms (e.g., Press et al. 1992). These complex-root solvers share the disadvantage that convergence is only guaranteed when the trial frequency is sufficiently close to a root. Challenges arise when pulsations become increasingly nonadiabatic because the trial frequencies (e.g., established from adiabatic eigenfrequencies, see Section 2) can be distant from the roots; consequently, the solver converges to the wrong root or does not converge at all. The result is an incorrect or incomplete nonadiabatic pulsation analysis.

To address this problem, we describe and apply a new "contour method" for generating initial trial frequencies. The contour method has two main benefits over other approaches. First, it successfully finds all nonadiabatic pulsation frequencies for tested stellar models and frequency ranges. Second, it generates a "contour map" that can be used to visualize the global nonadiabatic pulsation properties of a stellar model.

In Section 2 we review two approaches used by existing stellar pulsation codes to generate initial trial frequencies. In Section 3 we introduce the contour method and describe its implementation in the GYRE stellar pulsation code. In Section 4 we compare these various methods in calculating the nonadiabatic pulsation frequencies of three stellar models: 10 $M_\odot$ and 20 $M_\odot$ β Cephei stars, and a 0.9 $M_\odot$ extreme helium star. We show that the contour method finds nonadiabatic pulsation frequencies that are missed by other methods. In Section 5 we address the computational cost of the contour method, and discuss ways in which it can be mitigated. The contour method will be available in release 6.0 of the GYRE code, providing a new tool for modeling the unprecedented observational stellar pulsation data collected by the Transiting Exoplanet Survey Satellite (TESS; Ricker et al. 2014) and other future missions.

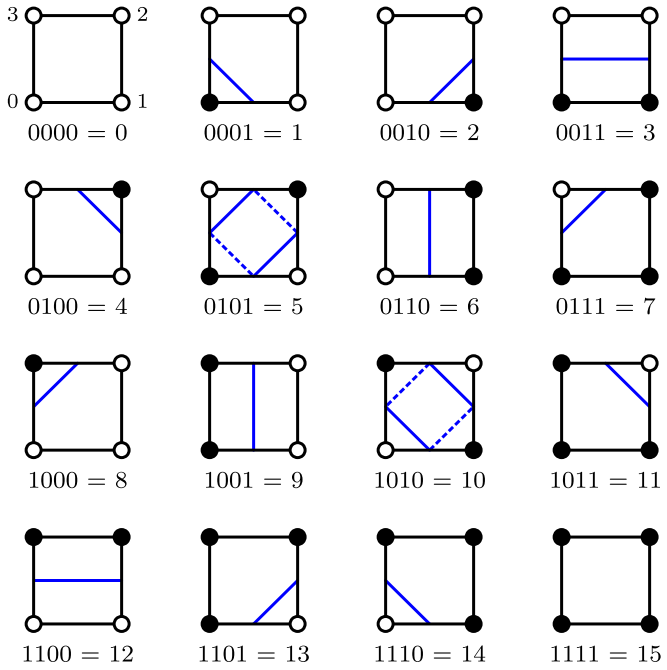

Figure 1. Look-up table for the marching-squares algorithm, showing the 16 possible configurations that can arise, and labeled by their index (in binary and decimal). Cell corners are plotted as circles; filled if the discriminant component ($\mathcal{D}_\mathrm{R}$ or $\mathcal{D}_\mathrm{I}$) is positive at that corner, and open if it is negative. Configuration 0 (top left) shows the labels $i = 0, \ldots, 3$ for each corner. The blue lines show example linear contour segments corresponding to each configuration. For configurations 5 and 10, there are two possible pairs of segments, shown using solid and dotted lines; GYRE adopts the pair with the shorter total length.

2. Background

2.1. Methods for Obtaining Initial Trial Frequencies

The most common approach for generating initial trial frequencies, which we call the "adiabatic method", is to first solve the LA stellar pulsation equations. This method is first described by Castor (1971), who constructs an adiabatic $\mathcal{D}(\sigma)$ and solves for its real-valued roots. The roots are perturbed, resulting in quasi-adiabatic frequencies that are used as initial trials for the complex roots of a corresponding nonadiabatic $\mathcal{D}(\sigma)$. Similar methods, using the unperturbed adiabatic roots, are implemented in the BOOJUM (Townsend 2005), LNAWENR (Suran 2008), and GYRE (Townsend & Teitler 2013; Townsend et al. 2018) nonadiabatic pulsation codes.

The adiabatic method, however, has a weakness. As a pulsation becomes increasingly nonadiabatic, that is, as the imaginary component of the frequency, σ_I, increases in magnitude, the real component of the frequency, σ_R, typically shifts away from the adiabatic frequency. As a result, the nonadiabatic frequencies can interlace the adiabatic ones. Consequently, when adiabatic roots are used as initial trial frequencies, the complex-root solver can converge to the nonadiabatic roots of neighboring modes, missing modes in the process. If pulsations are extremely nonadiabatic, that is, $|\sigma_I/\sigma_R| \gtrsim 1$, the nonadiabatic roots can be far enough from the adiabatic ones that the complex-root solver does not converge at all (see Section 4).

Another approach to generating initial trial frequencies, which we call the "minimum modulus method", was proposed by Gautschy & Glatzel (1990a). They construct a nonadiabatic $\mathcal{D}(\sigma)$ and evaluate its modulus, $|\mathcal{D}(\sigma)|$, as a function of σ_R to look for minima along the real axis ($\sigma_I = 0$). The values of σ_R at these minima then serve as initial trials for the complex roots of $\mathcal{D}(\sigma)$.

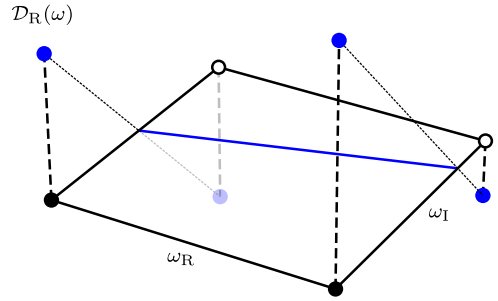

Figure 2. The linear interpolation process used to approximate where contour segments connect to cell edges. Illustrated here is the discriminant component $\mathcal{D}_\mathrm{R}$ for a cell with configuration 3 (see Figure 1).

The minimum modulus method, however, also has weaknesses. The first, similar to the adiabatic method, is that if pulsations are extremely nonadiabatic, some of the roots of $\mathcal{D}(\sigma)$ may be so far from the real axis that the complex-root solver does not converge (see Section 4). The second weakness is that because the method relies on the modulus of a complex function, there is a degeneracy of roots, which are complex conjugates. This was shown to occur in an extreme limit of nonadiabaticity associated with the strange instability (Gautschy & Glatzel 1990b).

3. The Contour Method

In the GYRE code, the contour method works by calculating a complex-discriminant function, $\mathcal{D}(\omega)$, on a grid in the complex-ω plane.[3] Here, ω is the dimensionless frequency, defined by

$$\omega = \sqrt{\frac{R^3}{GM}}\,\sigma, \tag{3}$$

where M is the stellar mass and R the stellar radius. This grid is then used to interpolate the zero-contours of the real and imaginary components of the discriminant, $\mathcal{D}_\mathrm{R}$ and $\mathcal{D}_\mathrm{I}$, respectively. The intersections between real and imaginary zero-contours approximate the roots of $\mathcal{D}(\omega)$ and serve as initial trial frequencies for the complex-root solver.

3.1. Constructing the Contours

We implement the contour method using the "marching-squares" algorithm (see, e.g., Wenger 2013), which generates zero-contours for a two-dimensional scalar field on a grid. First, a rectangular grid with a user-specified range and resolution in the complex-ω plane is constructed, and $\mathcal{D}(\omega)$ is evaluated at each grid point. This step can be computationally expensive, but it is ideally suited to parallel execution across a distributed cluster (see Section 5 for further discussion).

The zero-contours are then constructed by considering each rectangular cell defined by four adjacent grid points. These corner points are labeled in counter-clockwise order with an integer i, starting from $i = 0$ in the cell's lower-left corner. Each corner is

[3] We note that the contour method performs equally well using the dimensioned angular frequency σ in place of ω; however, most pulsation codes, including GYRE, work internally with ω.

assigned a value based on the sign of the discriminant component ($\mathcal{D}_{\rm R}$ or $\mathcal{D}_{\rm I}$) at its location: 2^i if the component is positive, and 0 if it is negative. The values for each corner are summed to determine a configuration index 0–15 for the cell.

This index is used to access a look-up table, illustrated in Figure 1, that specifies which cell edges should be connected by linear contour segments separating negative and positive corners. Cells with all positive corners (configuration 0) and with all negative corners (configuration 15) do not have any segments within them. Cells with diagonal pairs of negative and positive corners (configurations 5 and 10) are degenerate with two possible pairs of contour segments. GYRE chooses the pair with the shorter total length, but the degeneracy can be broken by constructing a higher resolution grid.

The location where a contour segment connects to a cell edge is approximated by a linear interpolation between the discriminant component values at the two corners. We illustrate this in Figure 2 for a cell with configuration 3.

3.2. Contour Intersections as Initial Trial Frequencies

In cells containing zero-contour segments of both $\mathcal{D}_{\rm R}$ and $\mathcal{D}_{\rm I}$, GYRE determines whether the segments intersect within the cell. If so, the intersection approximates where $\mathcal{D}(\omega) = 0$, and is adopted as an initial trial frequency for the complex-root solver. Figure 3 illustrates this process.

A powerful feature of the contour method is that when combined across cells, the zero-contour segments build a contour map that provides a rich visual representation of the global pulsation properties of a model across a given frequency range. We illustrate contour maps in the following section.

4. Calculations

In this section we compare and contrast the various methods for generating initial trial frequencies (Sections 2 and 3) in the context of β Cephei stars and extreme helium (EHe) stars.

β Cephei stars (e.g., Stankov & Handler 2005) are main-sequence stars with masses $M \gtrsim 8\,M_\odot$ that exhibit low-order pressure and gravity modes driven by the iron-bump κ mechanism (Cox et al. 1992; Dziembowski & Pamiatnykh 1993). The pulsations are weakly nonadiabatic, but increase in nonadiabaticity toward higher frequencies and higher masses.

EHe stars (e.g., Jeffery 2008) are rare, low-mass, high-luminosity, early-type supergiants that belong to a class of hydrogen-deficient carbon stars. It remains an open question how these stars became depleted of their hydrogen. EHe stars exhibit pressure modes and strange modes, driven by both the helium κ mechanism and by the strange-mode instability, which occurs in the presence of extreme nonadiabaticity.

We use release 12778 of the MESA stellar evolution code (Paxton et al. 2011, 2013, 2015, 2018, 2019) to construct models for 10 $M_\odot$ and 20 $M_\odot$ β Cephei stars, and for a 0.9$M_\odot$ EHe star; we describe these models in the following sections. We then apply the different methods for generating initial trial frequencies, implemented in GYRE to compare the resulting nonadiabatic pulsation analyses.

4.1. 10 $M_\odot$ β Cephei Star Model

The 10 $M_\odot$ stellar model is evolved from zero-age main-sequence (ZAMS) to the terminal-age main-sequence (TAMS), when the core hydrogen mass fraction, $X_{\rm c}$, drops below 10^{-5}. OPAL opacity tables are used with the protosolar initial abundances from Asplund et al. (2009), and we neglect any rotation or mass loss. Convection is modeled with a mixing-length parameter $\alpha_{\rm MLT} = 1.8$ without overshoot, and convective boundaries are determined using the predictive mixing scheme described in Paxton et al. (2018) with the Ledoux stability criterion.

We focus on a specific snapshot of the model chosen with $X_{\rm c} = 0.25$, which places it well inside the β Cephei instability strip for radial modes (e.g., Paxton et al. 2015, see their Figure 9). The parameters of this snapshot, and its position in the HRD, are shown in Figure 4 along with the star's main-sequence evolutionary track.

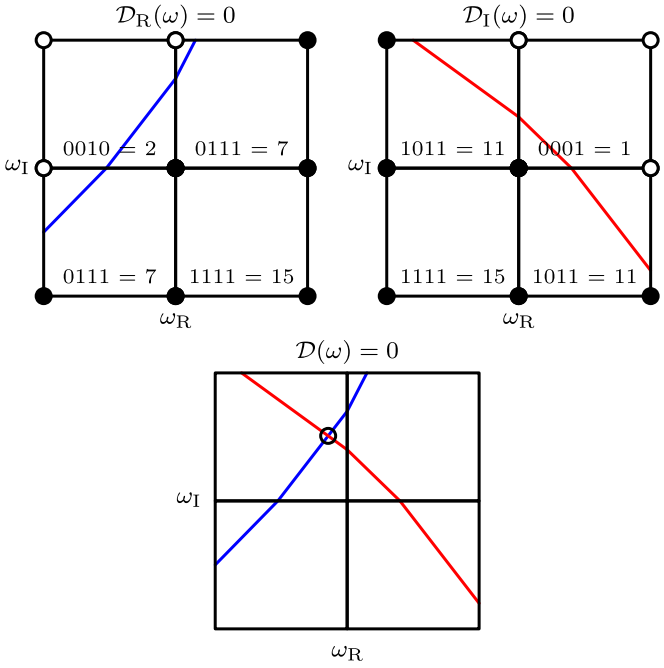

Figure 3. Top: an example grid showing cells labeled by their configuration index and corresponding zero-contour segments for discriminant component $\mathcal{D}_{\rm R}$ (left) and $\mathcal{D}_{\rm I}$ (right). Bottom: example contour intersection for $\mathcal{D}(\omega)$. The point in the top left cell where the segments intersect (highlighted with a circle) is an approximate root of $\mathcal{D}(\omega)$. The intersection serves as an initial trial frequency for the complex-root solver.

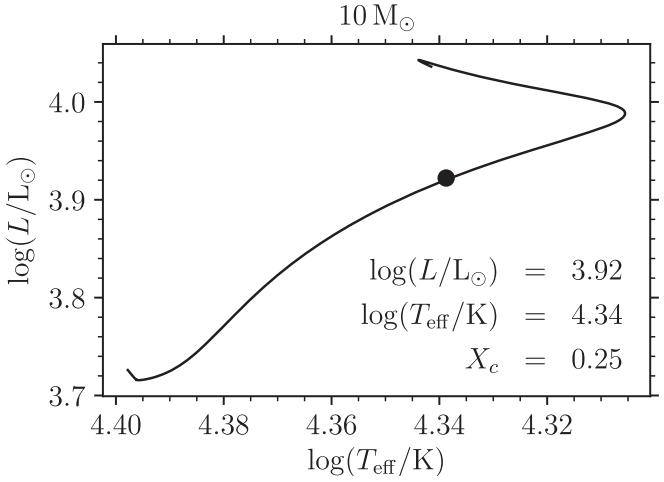

Figure 4. HRD showing the evolutionary track for the 10 $M_\odot$ β Cephei star model. The snapshot considered in the text is indicated by the filled circle, and labeled with its stellar parameters (luminosity, L; effective temperature, $T_{\rm eff}$; core hydrogen mass fraction, $X_{\rm c}$).

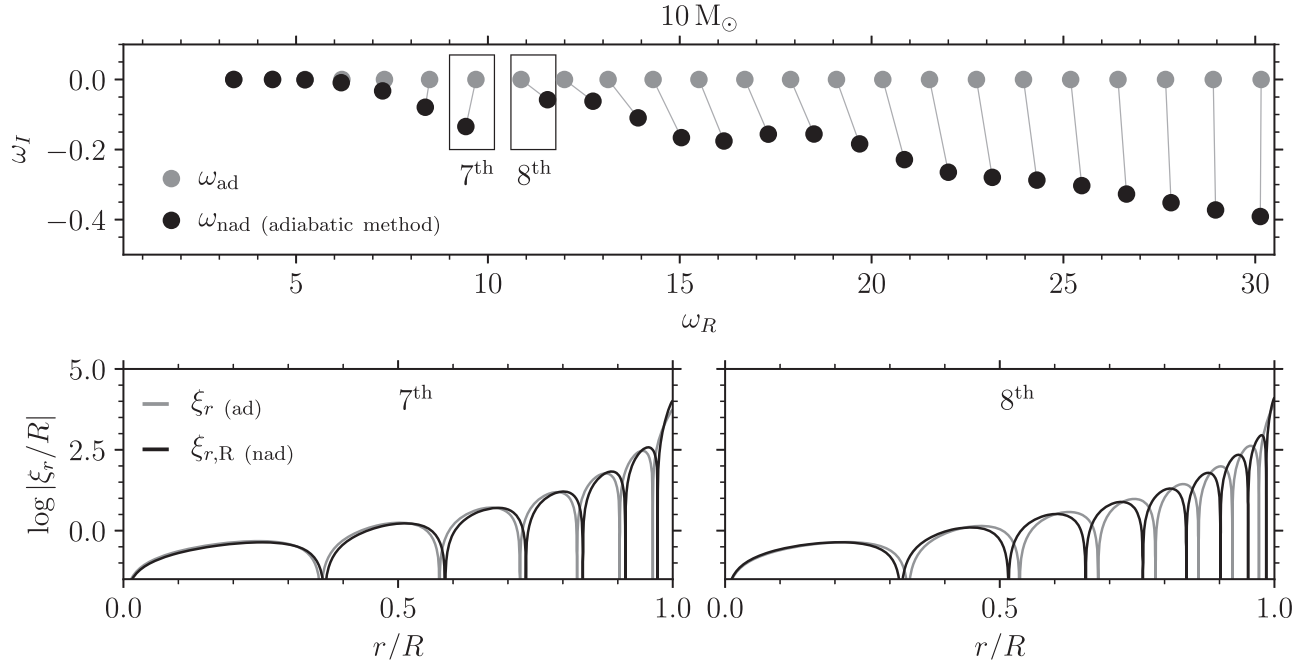

Figure 5. Top: dimensionless frequencies of radial modes in the complex-ω plane, found using the adiabatic method for the 10 $M_\odot$ snapshot marked in Figure 4. Lines join each nonadiabatic frequency ($\omega_{\rm nad}$, filled black circles) to the adiabatic frequency ($\omega_{\rm ad}$, filled gray circles) that was used as the initial trial frequency for the complex-root solver. Bottom: the dimensionless radial displacement wave functions, ξ_r/R, plotted as a function of fractional radius, r/R, for the frequencies boxed in the top panel (adiabatic, gray; nonadiabatic, black). In the nonadiabatic cases, we show only the real part of the wave function, $\xi_{r,\rm R}$. The wave functions for the 7th boxed frequency pair, shown on the left, exhibit 7 radial nodes for both adiabatic and nonadiabatic cases. The wave functions for the 8th boxed frequency pair, shown on the right, exhibit 8 radial nodes in the adiabatic case, but 9 in the nonadiabatic case. The nonadiabatic mode with eight nodes is missing.

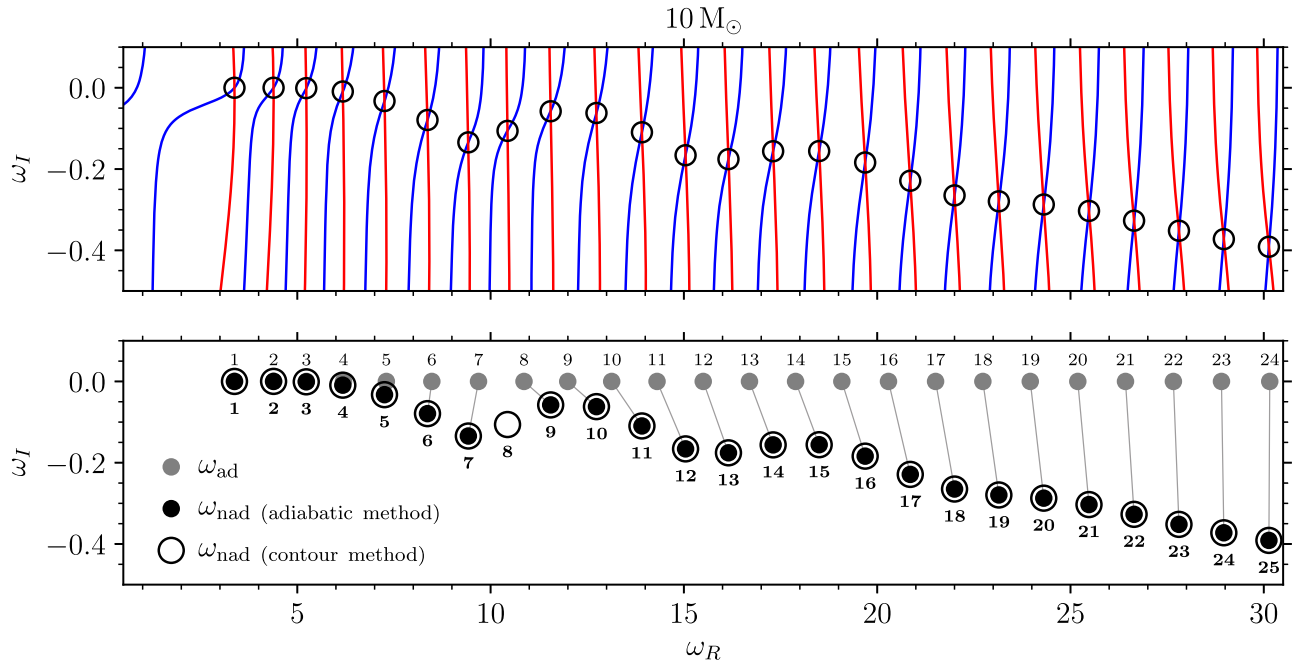

Figure 6. Top: contour map showing the zero-contours of the real ($\mathcal{D}_{\rm R}$, blue) and imaginary ($\mathcal{D}_{\rm I}$, red) components of the discriminant function in the complex-ω plane for the 10 $M_\odot$ snapshot marked in Figure 4. The intersections are approximate roots of $\mathcal{D}(\omega)$ and serve as initial trial frequencies for the complex-root solver. The open circles indicate the roots actually found by the solver. Bottom: dimensionless nonadiabatic frequencies of radial modes found using the contour method (open circles) overlaid on those found using the adiabatic method (gray and filled black circles, taken from the top panel of Figure 5). Each mode is labeled by the number of radial nodes in its radial displacement wave function. Note how the 8th nonadiabatic mode was missed by the adiabatic method.

4.1.1. Adiabatic Roots as Initial Trial Frequencies

We search for nonadiabatic radial modes of the 10 $M_\odot$ snapshot using the adiabatic method implemented in GYRE, and adiabatic frequencies in the range $0.5 \leqslant \omega_{\rm R} \leqslant 30.5$ as initial trial frequencies (the adiabatic method; see Section 2). In the top panel of Figure 5 we show the adiabatic and nonadiabatic dimensionless pulsation frequencies, $\omega_{\rm ad}$ and $\omega_{\rm nad}$, respectively, in the complex-ω plane. Lines join each nonadiabatic frequency

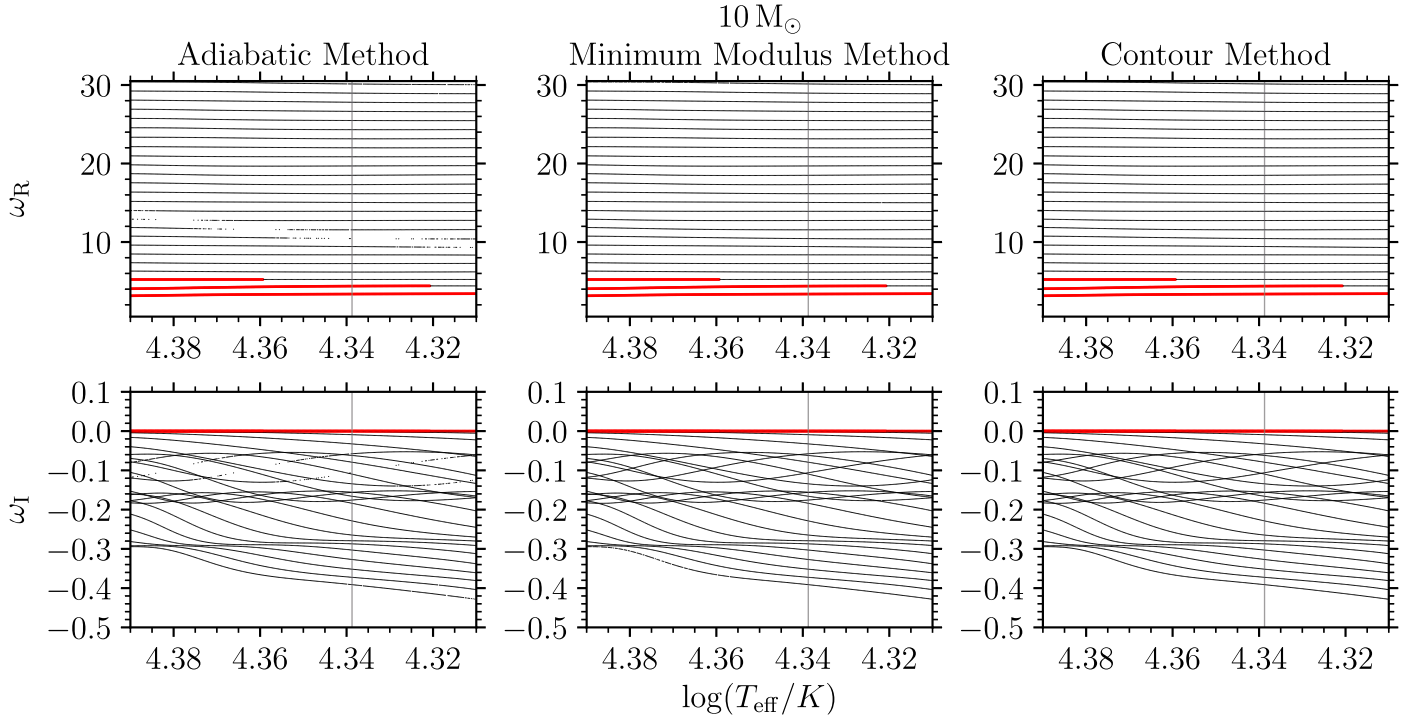

Figure 7. Modal diagrams showing the radial nonadiabatic frequencies (stable, black; overstable, red) of radial modes for the 10 $M_\odot$ model as it evolves across the main sequence. Top: the real part of the dimensionless pulsation frequency ω_R as a function of effective temperature, $T_{\rm eff}$; Bottom: the corresponding imaginary part, ω_I. The diagrams are constructed using the adiabatic method (left), minimum modulus method (middle), and contour method (right). The 10 $M_\odot$ snapshot shown in Figures 4–6 is indicated by a vertical gray line.

back to the adiabatic frequency that was used as its initial trial frequency.

Not immediately apparent in the figure is the fact that one of the nonadiabatic modes is missing. We see this when we examine the radial wave functions of modes with consecutive frequencies, expecting the wave functions to exhibit likewise-consecutive numbers of radial nodes.[4]

In the bottom panel of Figure 5 we plot the dimensionless radial displacement wave functions of the consecutive frequency pairs boxed in the top panel. In the nonadiabatic cases, we show only the real part of the wave function, $\xi_{r,R}$. For the seventh frequency pair, the adiabatic and nonadiabatic wave functions both show seven nodes, as we expect. For the eighth frequency pair, however, the adiabatic wave function shows eight radial nodes, but the associated nonadiabatic wave function shows nine. The nonadiabatic mode with eight radial nodes is missing. This illustrates the problem with using adiabatic frequencies as initial trial frequencies; the root solver does not always converge to the correct nonadiabatic ones.

To see which modes are missed as the 10 $M_\odot$ model evolves across the main sequence, we repeat our calculations for each timestep between the ZAMS and the TAMS. The left column of Figure 7 shows a modal diagram constructed from these calculations, plotting the nonadiabatic frequencies (upper panel: ω_R, lower panel: ω_I) of radial modes as a function of the effective temperature $T_{\rm eff}$. To improve the clarity of this and other modal diagrams, we only show models monotonically decreasing in effective temperature, neglecting the Henyey

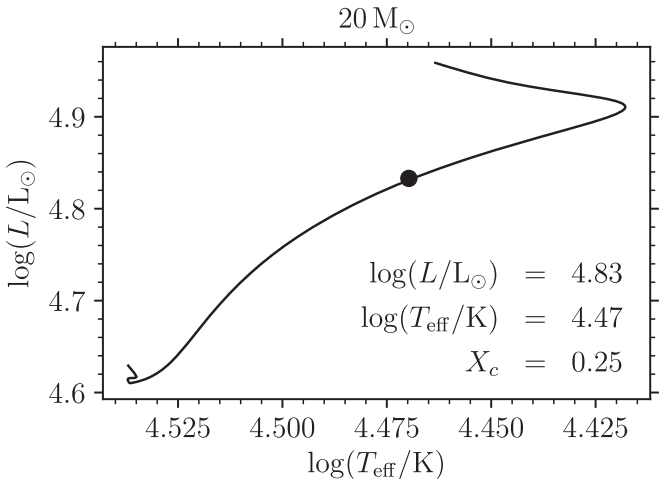

Figure 8. HRD showing the evolutionary track for the 20 $M_\odot$ β Cephei star model. The snapshot considered in the text is indicated by the filled circle, and labeled with its stellar parameters (luminosity, L; effective temperature, $T_{\rm eff}$; core hydrogen mass fraction, X_c).

hook portion near the TAMS when the star evolves to the blue in the HRD. Overstable modes are marked in red. A band of frequencies is missing, indicating where (as in Figure 5) the complex-root solver converged to the wrong nonadiabatic frequencies.

4.1.2. Minimum Modulus as Initial Trial Frequencies

For comparison, we repeat our calculations for the 10 $M_\odot$ model using the minimum modulus method (Section 2) implemented in GYRE. We show the resulting modal diagram in the middle column panel of Figure 7. The minimum modulus

[4] Strictly, this consecutive node numbering property applies only to solutions of the radial LA equations, which are of regular Sturm-Liouville form (e.g., Ledoux & Walraven 1958). However, in the present case, the radial modes are only modestly nonadiabatic, and so the property should also apply to the solutions of the radial LNA equations.

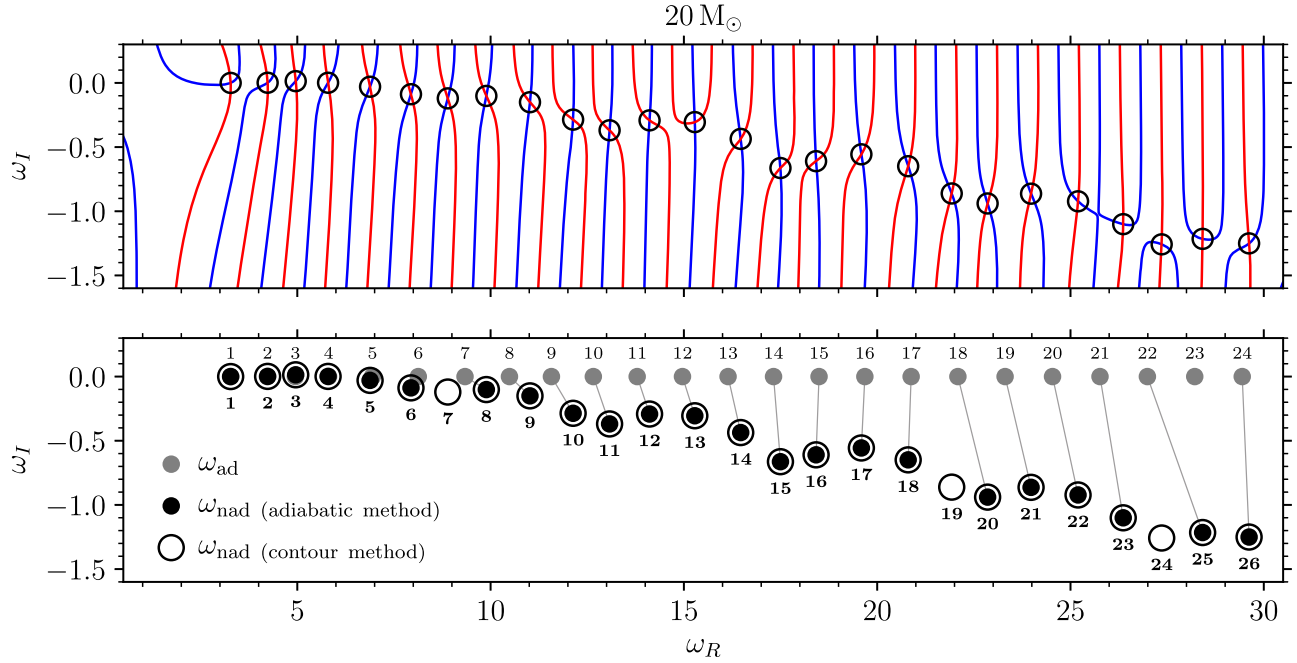

Figure 9. As in Figure 6, but the 20 $M_\odot$ snapshot marked in Figure 8 is shown. Note how three modes are now missed by the adiabatic method.

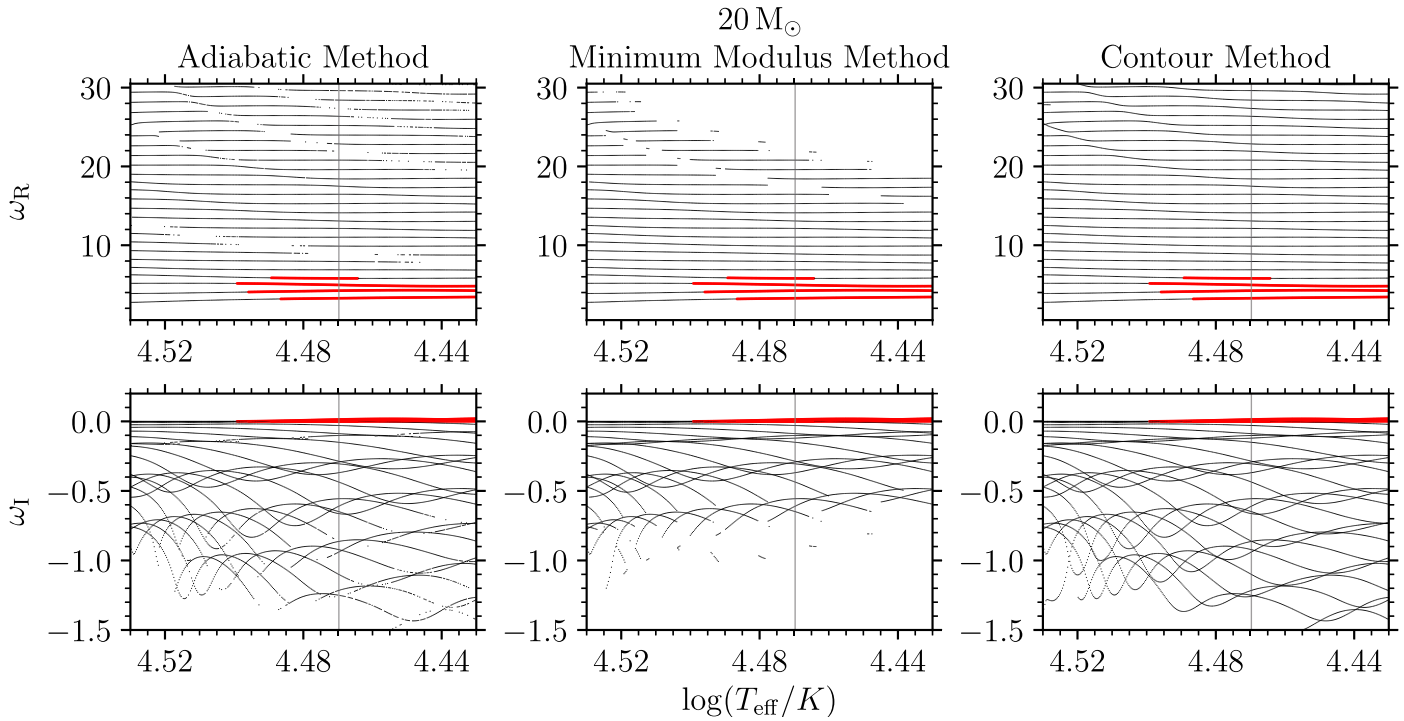

Figure 10. As in Figure 7, but the 20 $M_\odot$ model is shown.

method fills in the frequencies that were missed using the adiabatic method. This is because the nonadiabatic frequencies are close to the ω_R axis, and therefore produce well-defined minima in $|\mathcal{D}(\omega)|$ along this axis.

4.1.3. Contour Intersections as Initial Trial Frequencies

We again repeat our calculations for the 10 $M_\odot$ model, now using the contour method (Section 3) implemented in GYRE. We use a grid of 1000 points spanning $0.5 \leqslant \omega_R \leqslant 30.5$, and 400 points spanning $-6 \leqslant \omega_I \leqslant 6$, so that the grid spacing is the same in both dimensions. We show the contour map in the top panel of Figure 6, displaying the zero-contours of $\mathcal{D}_R$ and $\mathcal{D}_I$. The intersections of the contours are used as initial trial frequencies for the complex-root solver.

In the bottom panel of Figure 6, we compare the modes found using the contour method with those found using the adiabatic method, shown in the top panel of Figure 5. The contour method recovers all the modes previously found, but also finds the missing mode with eight radial nodes. We now see that with the adiabatic method, the eighth adiabatic frequency converged to the ninth nonadiabatic frequency.

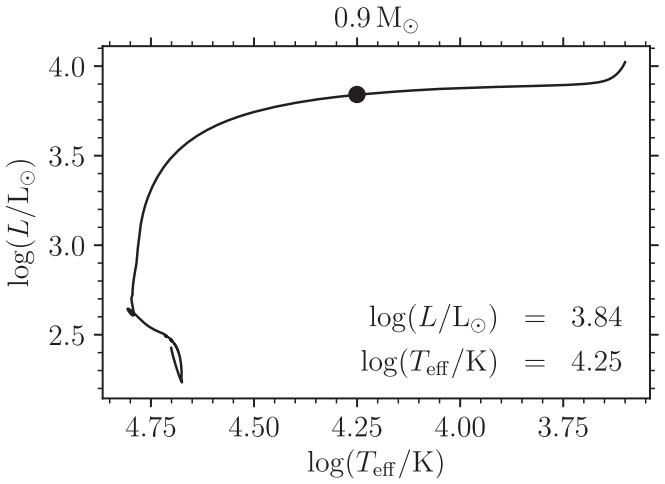

Figure 11. HRD showing the evolutionary track for the $0.9\,M_\odot$ EHe star model. The snapshot considered in the text is indicated by the filled circle, and labeled with its stellar parameters (luminosity, L, and effective temperature, $T_{\rm eff}$).

Each subsequent adiabatic frequency converged to the wrong nonadiabatic one. This highlights the problem with using adiabatic frequencies as initial trial frequencies even for weakly nonadiabatic pulsation. The contour method, on the other hand, provides initial trial frequencies that are close to the true roots, resulting in the robust convergence to all nonadiabatic frequencies.

We show the modal diagram for the contour method in the right column of Figure 7. The contour method fills in the frequencies that were previously missed when the adiabatic method was used. There is no difference between the modal diagrams for the minimum modulus and contour methods here for the $10\,M_\odot$ model, but—as we demonstrate below—the contour method still succeeds when the pulsations become strongly nonadiabatic and the other methods fail.

4.2. $20\,M_\odot$ β Cephei Star Model

We now repeat our analysis for a more massive $20\,M_\odot$ stellar model, calculated in the same manner as the $10\,M_\odot$ model. We begin by focusing on a snapshot chosen with $X_{\rm c} = 0.25$, as before, marked in Figure 8. Because its luminosity-to-mass ratio is higher, we expect the pulsations of this model to be more nonadiabatic than the $10\,M_\odot$ case (see, e.g., Saio et al. 1984).

In the top panel of Figure 9 we show the contour map for the $20\,M_\odot$ snapshot, along with the intersections that are used as initial trial frequencies. In the bottom panel of Figure 9, we compare the nonadiabatic frequencies found using the contour method with those found using the adiabatic method. The figure reveals that three nonadiabatic frequencies are missed using the adiabatic method.

In Figure 10 we show the modal diagrams for the $20\,M_\odot$ model constructed using the adiabatic method (left), minimum modulus method (middle), and the contour method (right). Multiple bands of frequencies are missed by the adiabatic method toward larger $\omega_{\rm R}$; the missing frequencies are apparently coincident with the avoided crossings. The minimum modulus method also experiences difficulties near avoided crossings, but it is additionally unable to find nonadiabatic frequencies with $|\omega_{\rm I}| \gtrsim 0.75$; this is because the minima in $|\mathcal{D}(\omega)|$ disappear as the roots become too distant from the $\omega_{\rm R}$ axis. Only the contour method finds all the nonadiabatic frequencies, as can be seen from the complete modal diagram.

4.3. Extreme Helium Star Model

The contour method is especially powerful for studying extremely nonadiabatic pulsations with high growth/damping rates ($|\omega_{\rm I}/\omega_{\rm R}| \gtrsim 1$). To demonstrate this, we repeat our analysis for a $0.9\,M_\odot$ EHe star model constructed to be qualitatively similar to the case studied by Gautschy & Glatzel (1990b, see their Figure 1). The model is created at the He-ZAMS with an initially uniform composition given by the mass fractions $X = 0$, $Y = 0.903$, $Z = 0.097$, and the R2 abundance profile from Weiss (1987); other modeling parameters are the same as for the β Cephei star models. It is evolved post He-TAMS until it reaches an effective temperature $\log(T_{\rm eff}/{\rm K}) = 3.6$. We first focus on the snapshot of the model chosen about half-way along its trip to the red, $\log(T_{\rm eff}/{\rm K}) = 4.25$. The parameters of this snapshot, and its position in the HRD, are shown in Figure 11 along with the star's evolutionary track.

In the top panel of Figure 12 we show the contour map for the $0.9\,M_\odot$ snapshot along with the intersections used as initial trial frequencies. In the bottom panel we compare the frequencies found using the contour method with those using the adiabatic method. The modes are more nonadiabatic than those of the β Cephei star models, and many frequencies are missed by the adiabatic method. The contour method, in contrast, robustly finds all frequencies. We see that there is no nonadiabatic mode with 27 radial nodes, which is a physical effect due to nonadiabaticity captured by the contour method, and not the result of a mode missed by the method.

In Figure 13 we show the modal diagrams for the $0.9\,M_\odot$ model, constructed using the adiabatic method (left), minimum modulus method (middle), and contour method (right). The diagrams are complicated, showing numerous avoided crossings and unstable strange modes; the extremely unstable mode around $\log(T_{\rm eff}/{\rm K}) \approx 3.8$ appears to correspond to the strange mode V found by Gautschy & Glatzel (1990b).[5] All methods capture some aspects of this complexity, but only the contour method results in a complete modal diagram.

5. Discussion

In this paper we introduce the contour method as a new way of generating initial trial frequencies that can be used to find the complex roots of a discriminant function, $\mathcal{D}(\omega)$, in the calculation of nonadiabatic stellar pulsations. The contour method involves evaluating the real and imaginary parts of $\mathcal{D}(\omega)$ on a complex-ω grid, constructing the zero-contours for each part, and then searching for contour intersections to serve as initial trial frequencies (Section 3).

We demonstrate the contour method implemented in the GYRE code by calculating nonadiabatic pulsation frequencies for $10\,M_\odot$ and $20\,M_\odot$ β Cephei star models, and for a $0.9M_\odot$ EHe star model (Section 4). Compared with the adiabatic method and with the minimum modulus method (Section 2), the contour method finds all the nonadiabatic pulsation

[5] Note that these authors used a minimum modulus method with more success than shown in our Figure 13; this could be a consequence of adopting a different discriminant function than GYRE.

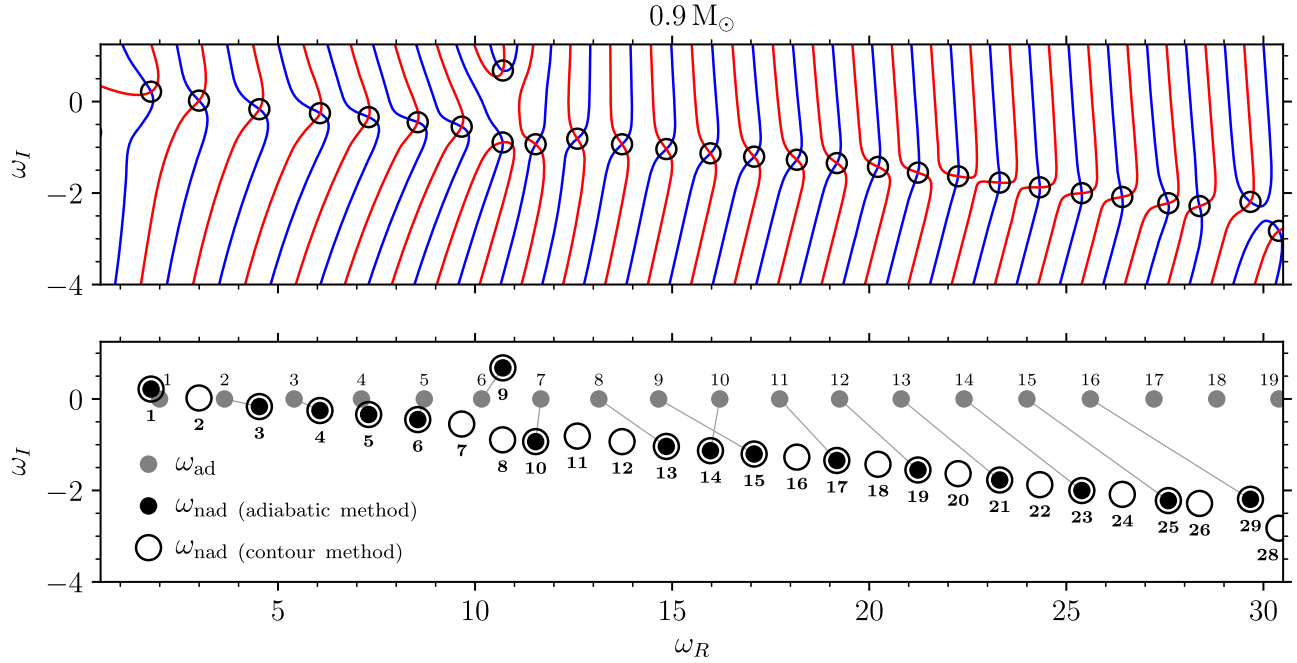

Figure 12. As in Figure 6, but the 0.9 $M_\odot$ snapshot marked in Figure 11 is shown. Note the increasing number of nonadiabatic modes missed by the adiabatic method, and that there is no nonadiabatic mode with 27 radial nodes.

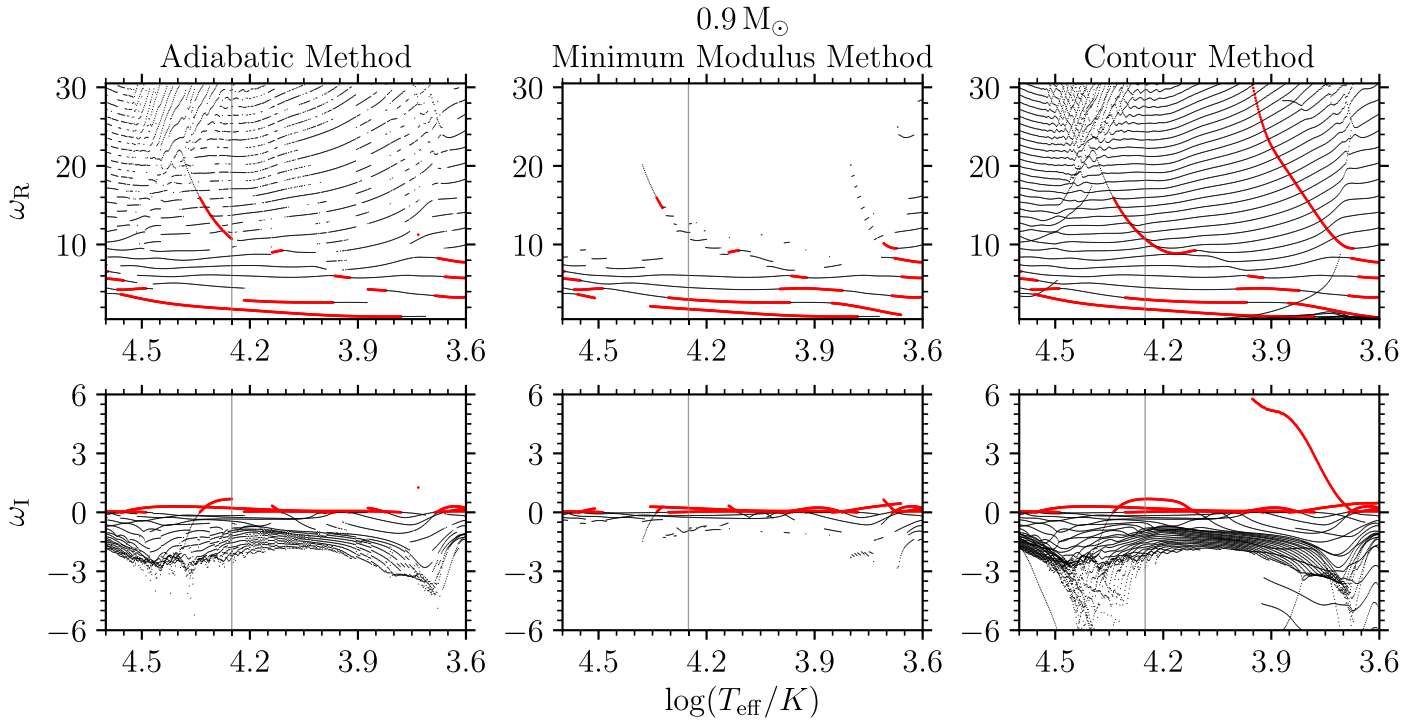

Figure 13. As in Figure 7, but the 0.9 $M_\odot$ model is shown.

frequencies within the given frequency range, especially as the modes become more nonadiabatic.

The contour method is not entirely novel; Dennis (1971) used plots of the zero-contours of a discriminant function in the complex plane to explore thermal instabilities of 15 $M_\odot$ He-shell burning models. However, the contour method has not been used for nonadiabatic pulsation problems, and it has not been automated using the marching-squares algorithm.

The contour method is also somewhat related to the method for finding initial trial frequencies described by Shibahashi & Osaki (1981). In their method, they map closed loops in the complex-ω plane to the complex-$\mathcal{D}(\omega)$ plane. A loop winding around a root in the ω plane will wind around the origin in the $\mathcal{D}(\omega)$ plane. If each loop is the size of a single grid cell, and if $\mathcal{D}(\omega)$ can locally be approximated as linear in ω, then it can be shown that the two methods become equivalent. The contour

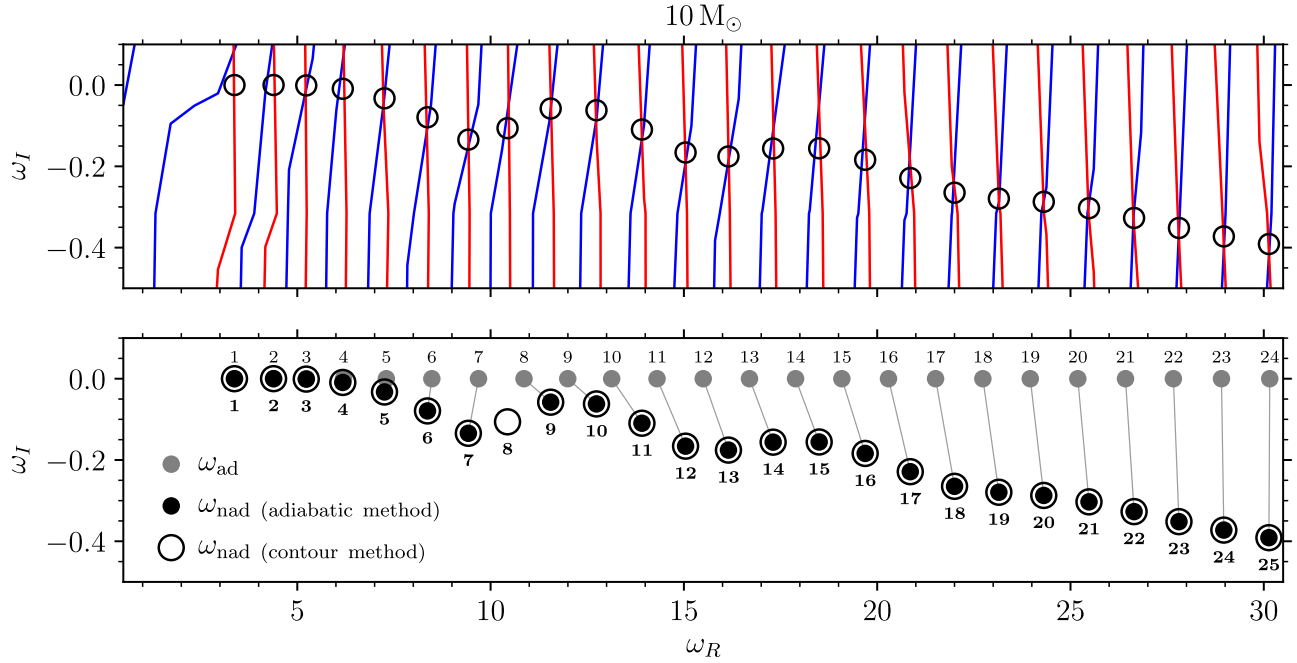

Figure 14. As in Figure 6, except that 20 times fewer points in $\omega_{\rm R}$ and $\omega_{\rm I}$ are used in creating the contour map. Note how the contour intersections in the upper panel no longer precisely coincide with the nonadiabatic frequencies.

method, however, has the additional benefit of creating maps that visually display the global nonadiabatic pulsation properties of a model.

The main drawback to the contour method is its computational cost. For the 10 $M_\odot$ snapshot considered in Section 4, the adiabatic method requires 31 s to calculate the modes shown in the bottom panel of Figure 6 (timings based on using a single core of a 2.60 GHz Intel E5-2690v4 processor). The minimum modulus method takes 102 s for the same calculation, and the contour method takes 300 minutes.

The expensive part of the contour method is evaluating $\mathcal{D}_{\rm R}$ and $\mathcal{D}_{\rm I}$ at every point on the grid. However, this expense can be mitigated in two ways. The first is that the evaluations are embarrassingly parallel and can take advantage of multiple cores and/or cluster nodes. Distributing the calculations across 28 E5-2690v4 cores via Message Passing Interface (MPI) calls reduces the calculation time of the contour method to 12 minutes, a nearly linear speedup. The second is that the contour method remains viable with a low-resolution grid; the contour map and the resulting intersections will be less accurate, but the intersections can still serve as sufficiently accurate initial trial frequencies. In Figure 14 we show the contour map and nonadiabatic pulsation frequencies found for the 10 $M_\odot$ snapshot, with 20 times fewer points than previously in both $\omega_{\rm R}$ and $\omega_{\rm I}$. The contour map is jagged and the pulsation frequencies found are no longer centered on the intersections, as in Figure 6, but the contour method still finds all nonadiabatic frequencies. With this grid resolution, the calculation takes 66 s on a single core, around 270 times faster than the original run.

The computational expense of the contour method means that it is not always the best approach to calculating pulsation frequencies. When nonadiabatic effects are very weak—for instance, in slowly pulsating B stars, whose gravity modes are characterized by low growth/damping rates—the adiabatic method for obtaining initial trial frequencies remains sufficient. However, for stars with higher growth rates such as the β Cephei and EHe stars modeled here, together with other pulsators at high luminosity-to-mass ratios, the contour method succeeds when the adiabatic method fails.

This is particularly relevant now as we expect unprecedented pulsation data from TESS (Ricker et al. 2014), which will observe the variability of high-luminosity stars previously excluded in directed campaigns (e.g., Kepler). These data, analyzed using the contour method, can be applied to model and test nonadiabatic pulsations across the HRD, providing fresh insights into stellar structure and evolution.

We thank Ellen Zweibel and Lars Bildsten for their insightful input during the project, and the anonymous referee for their helpful remarks. We acknowledge support from National Science Foundation grants ACI-1663696, AST-1716436 and PHY-1748958. This research was performed using the compute resources and assistance of the UW-Madison Center For High Throughput Computing (CHTC) in the Department of Computer Sciences. The CHTC is supported by UW-Madison, the Advanced Computing Initiative, the Wisconsin Alumni Research Foundation, the Wisconsin Institutes for Discovery, and the National Science Foundation, and is an active member of the Open Science Grid, which is supported by the National Science Foundation and the U.S. Department of Energy's Office of Science.

References

Aerts, C., Christensen-Dalsgaard, J., & Kurtz, D. W. 2010, Asteroseismology (Dordrecht: Springer)
Asplund, M., Grevesse, N., Sauval, A. J., & Scott, P. 2009, ARA&A, 47, 481
Castor, J. I. 1971, ApJ, 166, 109
Cox, A. N., Morgan, S. M., Rogers, F. J., & Iglesias, C. A. 1992, ApJ, 393, 272
Dennis, T. R. 1971, ApJ, 167, 311
Dziembowski, W. A., & Pamiatnykh, A. A. 1993, MNRAS, 262, 204
Gautschy, A., & Glatzel, W. 1990a, MNRAS, 245, 154
Gautschy, A., & Glatzel, W. 1990b, MNRAS, 245, 597

Jeffery, C. S. 2008, in ASP Conf. Ser. 391: Hydrogen-Deficient Stars, ed. A. Werner & T. Rauch (San Francisco, CA: ASP), 53
Ledoux, P., & Walraven, T. 1958, HDP, 51, 353
Paxton, B., Bildsten, L., Dotter, A., et al. 2011, ApJS, 192, 3
Paxton, B., Cantiello, M., Arras, P., et al. 2013, ApJS, 208, 4
Paxton, B., Marchant, P., Schwab, J., et al. 2015, ApJS, 220, 15
Paxton, B., Schwab, J., Bauer, E. B., et al. 2018, ApJS, 234, 34
Paxton, B., Smolec, R., Gautschy, A., et al. 2019, ApJS, 243, 10
Press, W. H., Teukolsky, S. A., Vetterling, W. T., & Flannery, B. P. 1992, Numerical Recipes in Fortran 77 (2nd ed.; Cambridge: Cambridge Univ. Press)
Ricker, G. R., Vanderspek, R. K., Latham, D. W., & Winn, J. N. 2014, AAS Meeting 224, 113.02
Saio, H., Wheeler, J. C., & Cox, J. P. 1984, ApJ, 281, 318
Shibahashi, H., & Osaki, Y. 1981, PASJ, 33, 427
Stankov, A., & Handler, G. 2005, ApJS, 158, 193
Suran, M. D. 2008, Ap&SS, 316, 163
Townsend, R. H. D. 2005, MNRAS, 360, 465
Townsend, R. H. D., Goldstein, J., & Zweibel, E. G. 2018, MNRAS, 475, 879
Townsend, R. H. D., & Teitler, S. A. 2013, MNRAS, 435, 3406
Unno, W., Osaki, Y., Ando, H., Saio, H., & Shibahashi, H. 1989, Nonradial Oscillations of Stars (2nd ed.; Tokyo: Univ. Tokyo Press)
Weiss, A. 1987, A&A, 185, 178
Wenger, R. 2013, Isosurfaces: Geometry, Toplogy, and Algorithms (Boca Raton, FL: Taylor & Francis Group)